Article:

Mamalis, D., Murray, J.J., McClements, J. et al. (2019) Novel carbon-fibre powder-epoxy composites: interface phenomena and interlaminar fracture behaviour. Composites Part B: Engineering, 174. 107012. ISSN: 1359-8368

https://doi.org/10.1016/j.compositesb.2019.107012

Novel Carbon-Fibre Powder-Epoxy Composites: Interface Phenomena and Interlaminar Fracture Behaviour

Dimitrios Mamalis*, James J. Murray, Jake McClements, Dimitrios Tsikritsis, Vasileios Koutsos, Edward D. McCarthy, Conchúr M. Ó Brádaigh

School of Engineering, Institute for Materials and Processes, The University of Edinburgh,
King's Buildings, Edinburgh EH9 3FB, United Kingdom

*To whom correspondence should be addressed: E-mail: d.mamalis@ed.ac.uk

Abstract

Carbon fibres with three different sizing agents were used to manufacture unidirectional composites based on a powder epoxy resin. Powder epoxy processing was investigated as a route for fast, cost-effective manufacturing of out-of-autoclave composites compared to more time-consuming vacuum infusion technologies. In this work, a heat-activated epoxy powder was used as a resin system in low-cost vacuum-bag-only prepregs for thick composite parts that are required in the renewable energy industry (e.g. wind turbine blade roots). The importance of interfacial bonding between fibres and the matrix is shown and the impact on the ultimate mechanical performance of the manufactured composites demonstrated. The surface characteristics of the sizing on the carbon fibres were investigated using atomic force microscopy (AFM) and Raman spectroscopy. Results showed that the amount of sizing on the fibres' surfaces was inextricably linked with surface roughness and coverage. This in turn influenced the mechanical and chemical interlocking phenomena occurring at the fibre/matrix interface. The composites' mechanical performance was evaluated using tensile, flexural and interlaminar fracture toughness tests. Fractographic analysis using optical and scanning electron microscopy (SEM) was likewise employed to analyse the fracture surfaces of the tested/failed composites. Interlaminar fracture toughness testing (DCB Mode-I) revealed that the interfacial adhesion differences could alter the fracture resistance of the composites, hence emphasizing the importance of the interfacial bonding strength between the polymer matrix and the carbon fibres.

Keywords:

A. Carbon fibre composites; B. Powder epoxy; C. Mechanical properties; D. Interface bonding

1. Introduction

In the last decades, polymers and fibre reinforced polymers (FRPs) have had a significant impact in numerous engineering applications by replacing traditional conventional materials such as steel or aluminium [1–3]. FRP properties can be customised by varying their form i.e., their laminate ply angles, stacking sequence, filler/fibre type and volume fraction [4–6]. Carbon fibres (CF) are one of the most extensively used reinforcement materials for the preparation of a large variety of composite parts in aerospace, marine and automotive industries when excellent mechanical properties in lightweight components are required [7–9]. They present unique advantages in terms of high specific strength and stiffness, performance-to-weight ratio, high thermal stability, high conductivity, self-lubrication and corrosion resistance [10–12]. In turn, the production of carbon fibre reinforced polymers (CFRPs) has generated considerable scientific and industrial attention due to their superior properties, which can provide high specific stiffness and strength, good damage tolerance and environmental resilience [13–16]. The matrix, or resin, used in CFRPs greatly affects the overall performance, most notably in-plane compression and shear, toughness, interfacial properties as well as thermal stability [17–19]. Low-viscosity thermoset resins such as epoxies and polyurethanes are commonly used for FRPs in industry due to their ease of processing. However, the manufacturing process has been shown to be a dominant factor in determining interfacial adhesion properties and the formation of voids present in a composite [3,20–25], hence governing the ultimate mechanical performance of the composite. At present, liquid thermoset processes have a number of disadvantages including long injection path lengths (resin infusion), uneven or incomplete wetting, and thermal runaway when deployed for processing of thick-section composite parts. All these disadvantages can be mitigated by the use of powder-epoxy type processes [26–30]. Breakthrough discoveries in the use of powder-epoxies as matrices in FRPs offer promising opportunities for new processing methods [26–32]. To this end, investigations were carried out by Maguire et al. and Mamalis et al. using numerical models for various processing conditions and different physicochemical characterisation techniques, respectively [27–30]. The authors demonstrated that composites based on powder-epoxy resins reinforced with glass or carbon fibre can effectively deliver new high quality and high performance materials, as a cost-effective alternative to manufacturing out-of-autoclave components for marine and wind applications.

It has been recognised that one of the important parameters determining the ultimate performance of CFRPs is the interface between the fibre and the matrix [33,34]. Good interfacial properties can improve integral mechanical properties of fibre-reinforced composites via reducing stress concentrations caused by load transfer from matrix to reinforcements [35,36]. However, the matrix is still the main factor in controlling the load transfer in composites [37,38] which determines the interfacial and the mechanical properties of composites. The interfacial adhesion is governed by both physical and chemical interaction phenomena. The former is mainly based on mechanical interlocking, and the latter is based on polar and acid-base linking [39,40].

Recently, Mamalis et al. investigated the effect of fibre straightness for different amounts (and types) of sizing on the mechanical performance of different CFRPs [28,30]. The authors fabricated unidirectional (UD) carbon fibre composites, with enhanced fibre straightness, based on a new powder epoxy technology. They demonstrated that the amount of sizing on the carbon fibre surface affected the fibre-fibre interactions between tows and plies which in turn improved the degree of fibre straightness. Furthermore, mechanical characterisation of the different CFRPs revealed a rather complex interface role, showing a competition between chemical and mechanical interlocking phenomena at the fibre/matrix interface. The fibre/matrix interface needs to be further investigated in order to deliver high performance UD CFRPs based on powder epoxies. Mulvihill et al. [41] studied the fundamental frictional behaviour of carbon fibres (same fibres as Mamalis et al. [30]) prior to manufacturing. The authors focused on tow-on-tow and tow-on-tool friction interactions, under different loading conditions, and subsequently on the effect of the adhesion properties between the fibres and the plies. Interestingly, the authors reported that the carbon fibre contact area increased with increasing volume of sizing; hence, higher friction forces resulted in higher adhesion strength being achieved. Furthermore, they showed that the directionality of the fibre-tows affected the friction coefficient, as parallel filaments achieved friction coefficients 1.7 – 3.2 times higher than those of perpendicular filaments [41]. The authors, however, stated that a contribution due to differences in sizing chemistry could not be ruled out.

This paper aims to investigate further the mechanical properties of powder epoxy based CFRPs, under tensioned conditions, with three different CF sizings i.e., the same carbon fibre family (T700SC) but different amount (and type) of sizing agent, as studied by Mamalis et al. [28,30].

Particular attention was paid to the topographical characteristics of the carbon fibre surface in terms of sizing roughness and surface coverage and also to the interfacial bonding between fibres and matrix. The surface properties of CFs were experimentally characterised using atomic force microscopy (AFM) and Raman spectroscopy. The tensile and flexural properties of the different CFRPs were measured and compared with the mechanical data published by Mamalis et al. [28,30]. Fractographic analysis using optical and scanning electron microscopy (SEM) was likewise employed to analyse the fracture surfaces of the tested/failed composites. Furthermore, the Mode-I interlaminar fracture toughness of powder epoxy laminates was extensively examined. Determination of the crack initiation and propagation characteristics as affected by the interface properties were specifically investigated. This research has been carried out as a part of an investigation to develop powder epoxy semi-prepreg materials, aimed at, but not limited to, the manufacturing of wind/tidal turbine blades using out-of-autoclave processes.

2. Experimental Procedure

2.1 Materials

A low melt viscosity multi-purpose powder epoxy resin with density 1.22 g/cm^3 at 25°C, (Grade EC-CEP-0016, supplied by EireComposites Teo), was used as the base matrix to manufacture the composite materials. The glass transition temperature range of the epoxy was between ~105°C (storage modulus onset) and ~125°C (tanδ peak)) [30]. Note that all initiators-reagents were pre-mixed in the powder epoxy. The curing reaction was heat-activated, and the supplier recommended a cure temperature between 170°C and 190°C. Commercially available continuous tow carbon fibres, T700S-24K, were provided by TORAYCA® (Toray Industries, Inc.). Three different types; 50C, F0E and 60E of the T700SC carbon family were used with 1%, 0.7% and 0.3% sizing agents (by weight), respectively [42,43]. Note that the mechanical and physical properties of the carbon fibres are the same. The average diameter of the carbon fibres was approximately 7 μm, and typical values of fibre tensile modulus and strength were about 230 GPa and 4.9 GPa, respectively, as specified by the manufacturer [42,43].

2.2 Fabrication of composites

Composite laminates, consisting of 5 plies (~1 mm thick) and 16-plies (~3 mm thick) measuring 450 × 250 mm (length × width) with the carbon fibres in the 0° direction parallel to the 450 mm side, were prepared manually by a hand lay-up technique. The thickness of a single cured ply was approximately 0.2 mm. A specially designed tensioning apparatus was adopted to apply tension to the carbon fibres during the cure cycle in order to enhance fibre-straightness and maintain the fibres in a steady formation, as reported by Mamalis et al. [28,30]. The carbon fibres (plies) were loaded in the tensioning apparatus, clamped at both ends and then tension was applied uniformly, as can be seen schematically in Fig. 1. It was assumed that the maximum force was achieved when the fibres started slipping at both clamped ends. Additionally, a newton meter (force-meter) was used to estimate the tension (force) applied on the carbon fibres and an approximate value of approx. 3000 N was measured. The epoxy powder was distributed evenly on each ply, using a paper strainer with a fine sieve filter, aiming towards a 60:40 (carbon: epoxy) final weight ratio of the laminate.

The curing of the CFRPs was performed under vacuum, and it consisted of 1) a drying stage at 50±1°C for ~400 min, 2) a β-stage; at 120±1°C for 60 min, and 3) a curing cycle with a ramping rate of 2±0.2°C/min up to 180±1°C, for at least 90 min. Then the laminates were allowed to cool to room temperature. Thermocouples (K-type) were placed at the edges and at the core of the lay-up to record the temperature profile during the thermal cycle as well as to ensure uniform heat distribution along the preformed laminate. The extraction of the testing coupons of all composites was conducted using a wet diamond saw. The cutting process was adopted to produce high quality smooth edges free from defects and imperfections that in turn might affect the final mechanical performance. The fibre volume fraction (FVF) and void content of all the processed composites were determined by the acid digestion method and by the matrix burn-off technique according to ASTM D3171 (2015) to assess the quality of the laminates produced. Additionally, neat epoxy plates were manufactured following the same thermal cycle as described for the composites to provide a baseline for comparison.

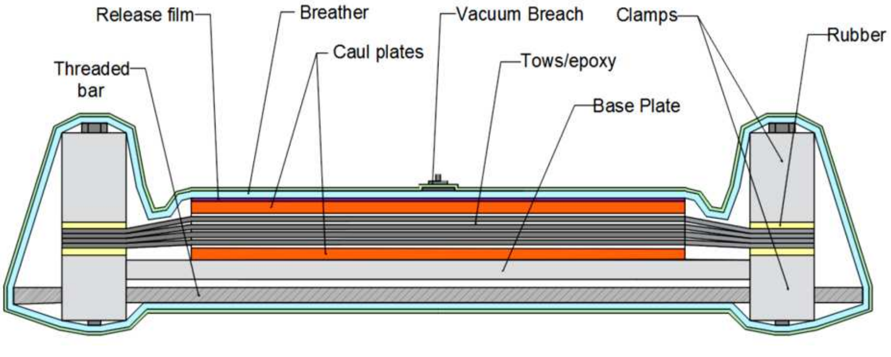

Fig. 1. A representative schematic drawing of the tensioning apparatus employed to manufacture CFRPs with enhanced fibre straightness.

2.3 Atomic Force Microscopy (AFM)

AFM experiments were performed to characterise the surfaces of the three different fibre types (50C, FOE and 60E) at the nanoscale. All imaging was carried out using tapping mode in air at ambient conditions with a Bruker Multimode/Nanoscope IIIa (Bruker, Santa Barbara, Ca, USA). RTESPA cantilevers purchased from Bruker were used for all imaging. The cantilevers had a nominal spring constant of 40 N/m, nominal resonant frequency of 300 kHz and a nominal tip radius of 8 nm. The sizes of the scans were small (1.2 x 1.2 μm^2) due to the small diameters and surface curvatures of the fibres. All image analysis was carried out using the freeware Gwyddion (http://gwyddion.net/) [44]. Height, amplitude and phase images were acquired for each fibre type. Additionally, profile plots were obtained showing the surface topography of the carbon fibres in greater detail. The profile plots were composed of horizontal line scans taken across the AFM images and their exact location was represented by horizontal bars on the corresponding height images. The profile plots and arithmetic average surface roughness (*Ra*) values were extracted and calculated, respectively, after the images had undergone flattening which reduced any influence from fibre curvature.

2.4 Raman spectroscopy

Raman spectroscopy was utilised to characterise the surface of the three different carbon fibre types (50C, FOE and 60E). The Raman system employed for this study was the LabRAM HR Evolution spectrometer supplied from HORIBA Scientific, Ltd. A diode-pumped frequency-doubled Nd:YAG laser with a wavelength of 532 nm was used. The 50X objective lens of an Olympus BH-2 optical microscope was used both to focus the laser beam on the samples and to collect the scattered light (NA=0.5). Note that there was no visible damage on the surface of the carbon fibre due to the laser. The grating used was 1800 grooves/mm for a window of 300-1900 cm^{-1}. For the detection, an Open Electrode CCD air-cooled camera was used to collect the Raman spectra. Samples, in the form of fibres were placed directly at the microscope stage, and the sample zone for the recording of spectra was selected optically. The obtained data were post-processed and analysed using Matlab 2015 software.

2.5 Tensile testing

Tensile tests were carried out in accordance with BS EN 2561 (1995) using a minimum of 12 specimens (dimensions: 250 length x 25 width x 1 mm thickness) for each composite family, i.e., 50C, F0E and 60E. End tab plates (100 mm x 50 mm x ~1 mm) of glass fibre reinforced epoxy (1581 type) arranged at ±45° were bonded using epoxy adhesive (2014-1 Araldite, Huntsman, UK) onto the end region of each specimen which had been previously grit-blasted. The tensile tests for composites and polymer specimens were performed in a universal testing machine Zwick/Roell, model Z250, with hydraulic grips and MTS 632.85F-14 extensometer, at constant cross-head speed of 2 mm/min. The test machine and 250kN load cell were calibrated in accordance with ISO 7500-1 (2015) and ASTM E4 (2016) standards. The fitted extensometer was calibrated in accordance with ISO 9513 (2012) and ASTM E83 (2016). Furthermore, the tensile properties of the neat epoxy were determined according to ASTM D638 (2014) standard. Epoxy plates with approximate thickness of ~3 mm were manufactured and subsequently cut based on the Type II (dog-bone) specimen.

2.6 Flexural testing

The flexural properties (strength and modulus) of the composites and the neat epoxy resin plates were investigated on a universal testing machine Zwick/Roell, model Z010, using a four-point bending fixture at a cross-head speed of 1 mm/min, at room temperature, according to ASTM D7264 (2007). A 10 kN load cell was used where the calibration and verification of the measuring system load cell was based on ISO 7500-1:2015 and ASTM E4-2016 standards. The specimen thickness ranged between 3 and 4 mm following a span-to-thickness ratio of 32:1, a standard specimen width of 13 mm, and a specimen length of around 20% longer than the support span. The diameter of all the loading noses was 4 mm. A linear variable differential transducer (LVDT), supplied from RDP Electronics Ltd, was fitted to measure the absolute linear displacement (position). A minimum of six samples for each composite or neat epoxy type were tested. The relative error of the measurements was estimated to be ~7% based on reproducibility of the resulting data.

2.7 Optical Micrographs and Scanning Electron Microscopy

Microstructural observation of the fabricated composites was carried out by optical microscopy (Zeiss Axioskop 2 Plus Ergonomic Trinocular Microscope). Optical microscopy specimens were embedded in transparent phenolic resin, followed by automated grinding and polishing. The surface morphology and the failure mechanism of the fractured composites (flexural specimens) were examined at the nanoscale using a Hitachi S-4700 field emission scanning electron microscope (FE-SEM) with an excitation voltage of 5-20 kV. Prior to examination, all the fracture surfaces were cleaned with ethanol to eliminate impurities such as dust. Then the CF/epoxy samples were sputter-coated with a thin evaporated layer of gold for a period of 5-8 min reaching a thickness of approximately 100 Å to improve conductivity and prevent charge build-up by the electrons absorbed by the specimen during the SEM examination. The failed flexural specimens were cut along the length of the specimen, polished and observed under an optical microscope to indicate the types of failure that occurred and to determine the degree to which each failure mode contributed. However, the fracture surface could not be observed using SEM without completely separating the two sample halves.

2.8 Double Cantilever Beam (DCB) tests

To evaluate the interlaminar properties of the prepared laminates, Mode I (G_{IC}) interlaminar fracture toughness tests of the three types of laminates were performed. Mode-I DCB tests were conducted in accordance to the ASTM D5528-13 standard using an Instron universal testing machine (Model 3369) and a 1 kN load cell. The Mode-I tests were carried out at a quasi-static cross-head displacement rate of 1 mm/min, and at least five specimens for each fibre type composite were tested. A 13 μm PTFE film was inserted in the mid-plane of the laminate; between the 8th and 9th plies (18 plies total), at a right angle to form an initial crack with a nominal delamination length of $a \approx 63$ mm from the load line. The manufactured laminates were carefully machined to extract testing specimens with dimensions of 150 mm length, 25 mm width and nominal thickness ~3.3 mm. Prior to testing, a white marker was applied at the edges of the specimens, and the samples were speckle patterned to measure the crack growth during testing. A tensile load was applied through two loading blocks adhered to the end of each specimen, and video extensometry (UVX - Imetrium systems) was applied to record the crack initiation and propagation for each test. The camera incorporated into the system was a Manta G-146B/G-146C, capable of logging at 17.8 frames per second. The Mode-I interlaminar fracture toughness, G_{IC}, was calculated using the modified beam theory according to ASTM D5528 standard, taking into account the rotation at the delamination front, as follows:

$$G_{IC} = \frac{3P\delta}{2b(a+|\Delta|)} \qquad (1)$$

Where P is the load, δ is the displacement, b is the specimen width, a is the delamination length, and Δ is the horizontal axis intercept from the linear $a - C^{1/3}$ curve. The compliance, C, is the ratio of displacement to corresponding load, δ/P. The initial value of G_{IC} was obtained as the average of G_{IC} values at the 50 mm delamination length.

3 Results and Discussion

3.1 Surface topography

Atomic force microscopy was utilised to characterise the surface morphology of the three carbon fibres at the nanoscale as well as quantify the surface roughness [36,45–51]. Additionally, the topographical characteristics of desized carbon fibres were also investigated as a baseline and by means of comparison. The Soxhlet method was used to extract the sizing agents from all the carbon fibre surfaces, which was conducted with acetone at 80°C for ~24 h with about 1 m fibre in length, for each carbon fibre type. Typical AFM images obtained from the desized surface of the carbon fibre can be seen in Fig. 2 where (A) is a height image with the respective (B) profile plot, whilst (C) and (D) are amplitude and phase AFM images, respectively. The AFM images show very little topography on the desized fibres' surfaces and the calculated average surface roughness R_a value was to found to be ~2.6 nm indicating a very smooth carbon surface. In Fig. 3, typical AFM height images with accompanying profile plots for each sized fibre surface are presented. More specifically, Fig. 3(A) presents the surface of the 50C fibre, which is dominated by polymeric agglomerates owing to the highest amount of sizing agent (1%) on the surface of these fibres. The presence of individual agglomerates can be clearly observed in the profile plot in Fig. 3(B) where the maximum height and width values were found to be approximately 100 nm and 500 nm, respectively. Furthermore, the 50C fibre revealed a relatively rough surface with a calculated $R_a$value of ~13.3 nm. Fig. 3(C) presents a typical height image of the F0E fibre case where there is a large number of agglomerates on the surface. The profile plot in Fig. 3(D) indicates that the observed polymeric agglomerates generally had lower height values than those of the 50C fibre case. The measured R_a value of the F0E case was ~9.1 nm. The agglomerates were elongated and the maximum height and width values were approximately 40 nm and 600 nm, respectively. The height image of the

60E fibre (Fig. 3(E)) shows a much smoother and cleaner surface. The profile plot for the 60E case was far less distinctive than the respective plots for the 50C and F0E case, as can be seen in Fig. 3(F). The agglomerates had maximum height and width values of approximately 30 nm and 220 nm, respectively. The surface was significantly smoother than the 50C and F0E fibres cases with a R_a value of ~3.2 nm. A summary of all surface roughness $R_a$values obtained from AFM imaging are presented in Table 1. Note that AFM measurements on the external surface of all the sized fibres as well as the desized ones, were performed in multiple locations (4 or more) on different fibres. AFM surface measurements indicated that there was a direct correlation between the amount of sizing on the external fibre surface and its surface roughness. Thus, this could essentially affect interface interactions between the fibre and the matrix.

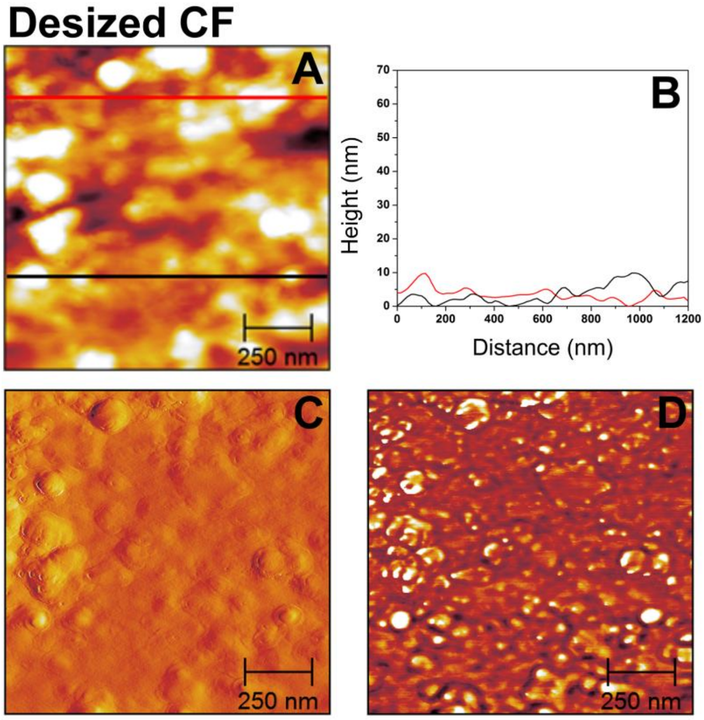

Fig. 2. Typical AFM (A) height images with the respective (B) profile plot, (C) amplitude and (D) phase images for the desized carbon fibre. The area of each line scan in the profile plots is represented by the horizontal bars in the corresponding height image.

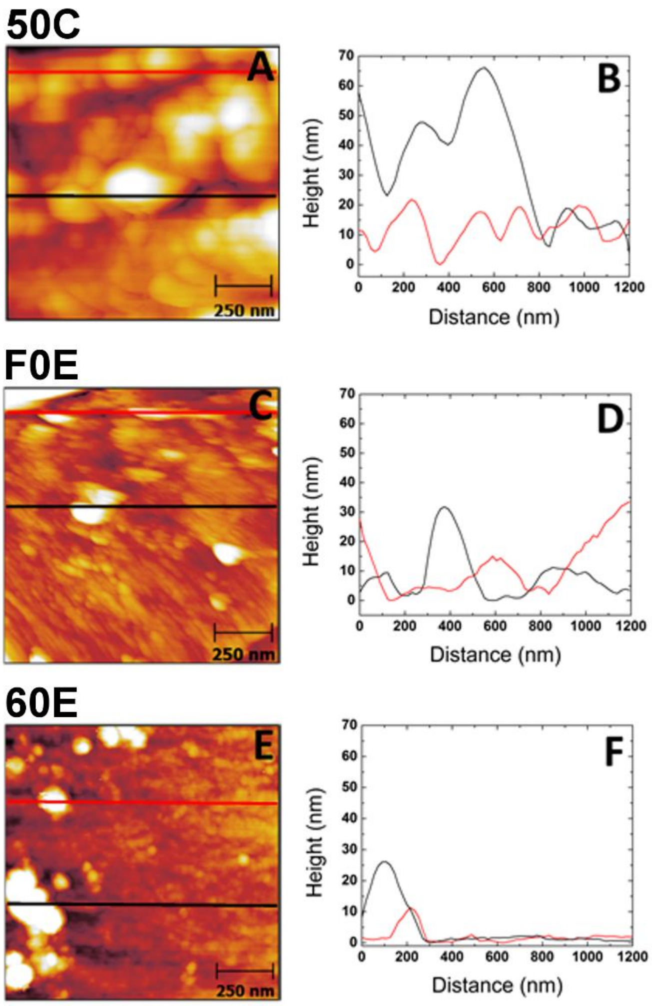

Fig. 3. AFM height images and respective profile plots for the three fibre types. The area of each line scan in the profile plots is represented by the horizontal bars in the corresponding height image. Note that (A) and (B) present a typical height image and profile plot of the 50C fibre, respectively; (C) height image and (D) profile plot of the F0E fibre case while (E) and (F) show a height image and profile plot of the 60E fibre, respectively.

Table 1 Summary of AFM surface roughness R_a measurements.

Carbon fibre (T7000SC)	R_a **(nm)**
Desized CF	2.6 ± 0.2
50C CF	13.3 ± 2.2
F0E CF	9.1 ± 0.9
60E CF	3.2 ± 1.3

Fig. 4 shows AFM amplitude and phase images for each sized fibre type. Amplitude images can be used to gain a better understanding of surface morphology by displaying clear edge detection although they cannot provide quantitative data in the z-direction. Phase images use colour contrast to display any differences in the phase angle during imaging. The phase angle is determined by the viscoelastic properties of a sample's surface, and therefore, can provide information regarding the composition of materials within a sample [52]. However, colour contrast in phase images can also be influenced by topography [53]. In this study, phase images were used to provide qualitative information regarding the composition of materials on the fibres surfaces. The amplitude image of the 50C fibre (Fig. 4(A)) clearly shows the presence of visible polymeric agglomerates on the fibre surface. Their size and shape varied significantly, some were rounded whilst others had much straighter edges. The phase image of the 50C fibres in Fig. 4(B) showed distinctive contrast differences in some areas. However, these areas were located where the surface had the largest height values, thus indicating that the variations in phase angle were caused by surface topography only. There was very little contrast in areas without varying topography, demonstrating that the viscoelastic properties of the surface were mostly homogenous [53]. In Fig. 4(C), the amplitude image of the F0E fibre shows that the elongated polymeric agglomerates varied in size and also formed distinct longitudinal lines (streaks) across the fibre surface, originating from the manufacturing process. These lines were mostly orientated at angles of 45°, although, this value varied in the upper right corner of the image. The phase image of the F0E fibre (Fig. 4(D)) showed contrast only where variation in topography was observed. There was little contrast elsewhere on the surface, which suggested the viscoelastic properties were mostly homogenous. The amplitude image of the 60E fibre (Fig. 4(E)) shows that agglomerates were sparsely arranged on the surface. A small proportion of the surface had a denser arrangement of agglomerates, such as the bottom left corner of the image. All contrast in the phase image for the 60E fibre (Fig. 4(F)) was located in the denser areas of agglomerates, suggesting the contrast was due to topography alone and the viscoelastic properties of the surface were fairly homogenous. It is well established that the interfacial bond strength between fibres/matrix depends to a great extent on the carbon fibre surface [48,54]. Comparison of the AFM images of the carbon fibres demonstrated that the sizing agent amount appeared to greatly affect the external fibre surface topography. In turn, the increased surface roughness due to the sizing agent on the carbon fibres is believed to enhance the mechanical interlocking phenomena (as well as the chemical interlocking) between fibre and matrix, by favourably improving interfacial bonding.

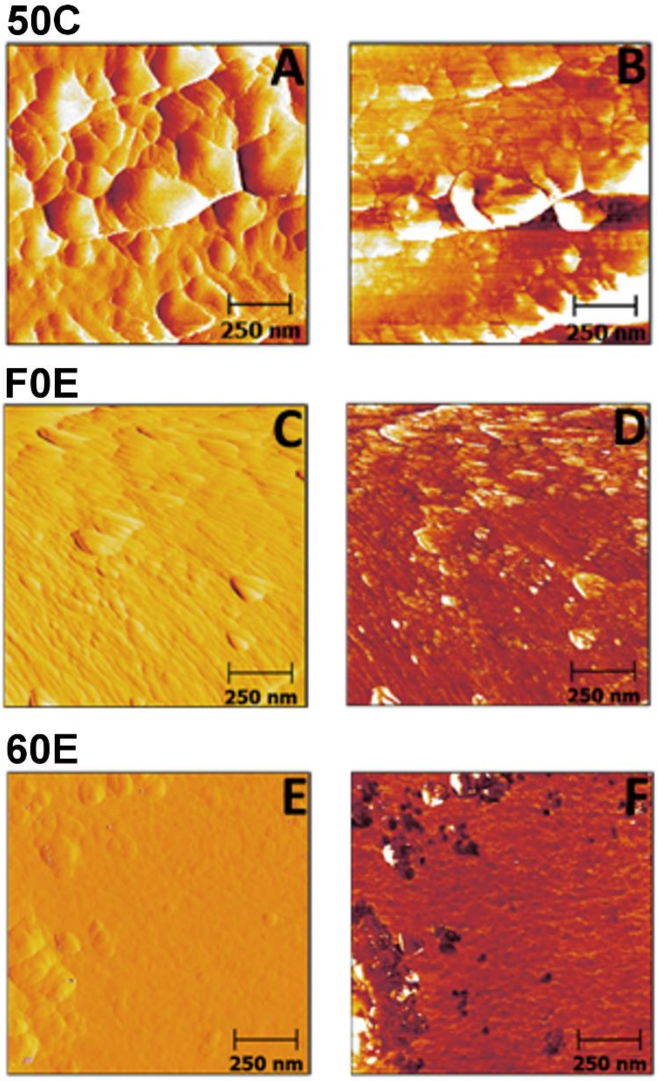

Fig. 4. Typically AFM amplitude and phase images for the three fibres types. (A) and (B) depict amplitude and phase images of the 50C fibre, respectively. (C) presents an amplitude image and (D) shows a phase image of the F0E fibre case. (E) and (F) refers to the amplitude and phase images of the 60E fibre, respectively.

3.2 Raman analysis

Raman spectroscopy has been utilised extensively to a wide range of carbon materials from graphitic [55,56] to amorphous carbon materials [57,58] and it can be used to characterise their nanostructure [59]. Raman spectroscopy can detect signals from a few microns in depth in materials and the obtained Raman spectra show characteristics of the state of graphitisation of the material. In addition, it can also be used as a technique for studying the variation of microstructures across carbon fibres i.e., crystallites and the disordered density in the carbon fibres [59]. Reproducible spectra were obtained for the three carbon fibres, with distinct, active

Raman bands from literature identified using a 532 nm incident laser. While these carbon fibres have the same fibre core (T700SC family), they have been coated with different amounts (and types) of epoxy resin [30,42,43] and in turn differences in the obtained spectra are expected. Fig. 5 shows the Raman spectra for the three different types of carbon fibre i.e., 60E (0.3%), F0E (0.7%) and 50C (1%), used in this study. Two main characteristic peaks, namely D and G, can be observed at approximately 1380 cm^{-1} and 1580 cm^{-1}, respectively [60]. More specifically, the D band peak represents structural defects (amorphous graphite), while the G band peak referred to integral graphite structure (crystal boundaries) of the graphite crystallites on the fibre surface [60–62]. The ratio of the intensities of the D and G peaks corresponds to the ratio of the defect density to the crystalline graphite [61,63]. However, the shape of the carbon fibre spectrum may change depending upon the excitation wavelengths [59]. The intensities of the latter peaks were calculated by applying a Lorentzian fit over the Raman spectrum for each peak. Then, the peak intensity ratio of the two bands I_D/I_G was calculated for each fibre case. A higher value of I_D/I_G indicates a higher defects density on the carbon fibre surface [45]. The 50C, F0E, and 60E fibres exhibited I_D/I_G ratios of approx. 0.96, 0.94 and 1.02, respectively. The 60E fibre shows greater surface defects than the F0E and the 50C coated carbon fibres. The highest amount of applied epoxy-type sizing [28,30,43] on the 50C carbon fibres has reduced the amount of detectable defects. Similar findings were obtained for the F0E case (i.e. the amount of sizing has reduced the amount of detectable defects compared to 60E) but more prominent surface defects were detected than the 50C carbon fibre case which carries the highest amount of sizing. More surface defects were detectable in 60E compared with the other cases. Note again that the amount of sizing agent on the carbon fibre surfaces decreased in order of the following sequence of treatments 50C>F0E>60E. The latter trend was indicated by absorbance decreasing in the same order, which was indicated by a decreasing number of counts (Fig. 5), supporting the AFM topography measurements (Figs. 3 and 4) as well as with the FTIR results reported by Mamalis et al. [30]. The varying surface coverage due to the different thicknesses (amounts) of the applied polymer coatings on the three fibres have affected the Raman signal intensities, and this will in turn indicated different defects at the carbon surface. In summary, the carbon fibre surface is always the same; it is the surface coverage of the sizing that affects the Raman signal coming from the carbon fibre surface. Furthermore, it should be noted that another technique to study these type of defects would be Tip-Enhanced Raman Scattering (TERS), which would allow a direct correlation of the surface topography with the local density of defects measured via Raman spectra at a higher spatial resolution [63]. However, this is beyond the scope of this current work.

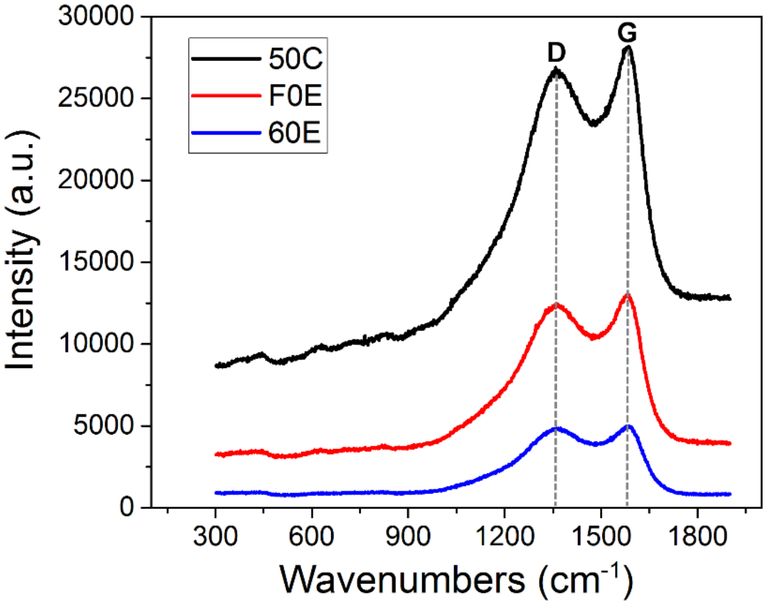

Fig. 5. Raman spectra of the three different carbon fibre types i.e., 50C (black), F0E (red) and 60E (blue).

3.3 Tensile properties

One of the most fundamental parameters that controls the properties of fibre/epoxy composites is the fibre content. Stiffness and strength as well as other properties, depend essentially on the fibre content and orientation [30]. Thus, the fibre volume fraction (FVF) and the consolidation quality, in terms of uniformity and void content of the produced laminates, were measured by acid digestion and matrix burn-off methods in accordance to ASTM D3171 (2015). Fig. 6 shows a summary of the results obtained from the fibre volume fraction and void content (volume) calculations by applying these two techniques. Overall, the average FVF and void content values were calculated to be 58±3% and 1.1±0.2%, respectively, for all examined composites. Note that three or more laminates (and a minimum of three tests) for each of the three composite cases were examined in order to inspect the consistency of the fabrication process. It is clear from Fig. 6 that the slight FVF variations observed between the same families of composites indicated good material uniformity and reproducibility. Furthermore, the characteristically low and invariable void contents (Fig. 6), highlights the excellent consolidation quality and absence of voids for all tested composites.

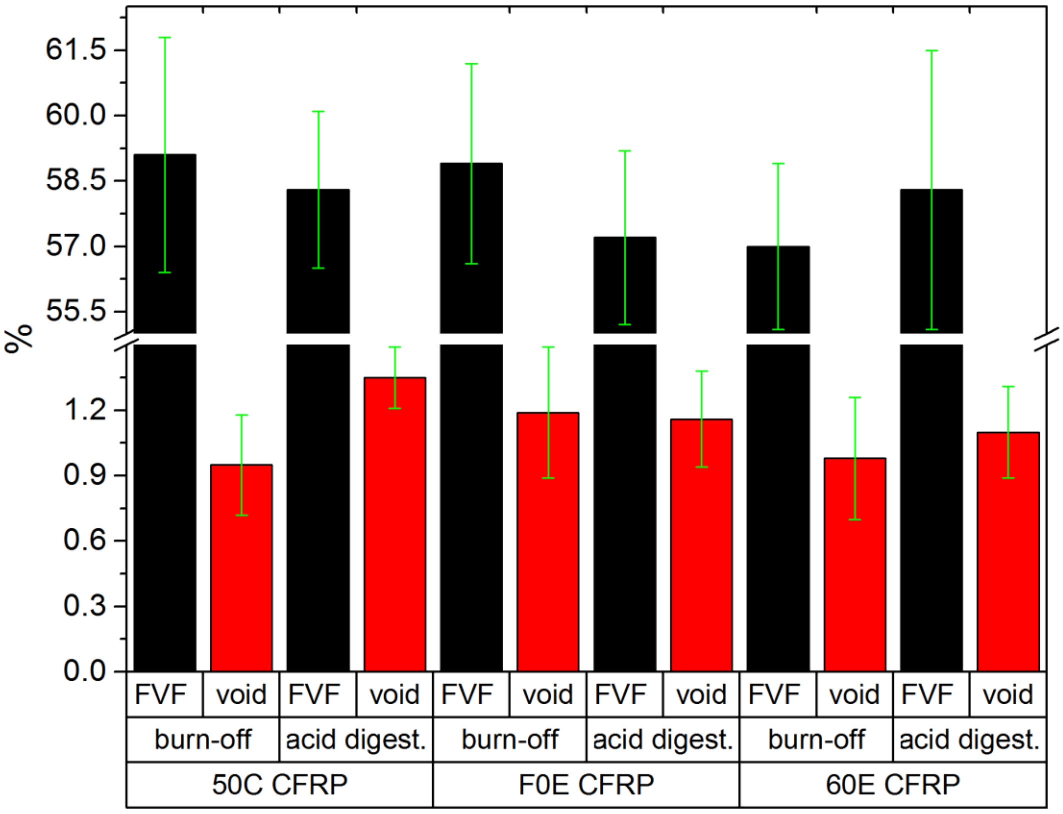

Fig. 6. Average fibre volume fraction (FVF) and void content calculations for all manufactured composite cases by applying matrix burn-off and acid digestion methods according to ASTM D3171 (2015). Note that three or more laminates (and a minimum of three tests) for each composite family was examined.

In what follows, the tensile properties of the three UD composites and the neat (powder) epoxy, are presented in Table 2. The tensile tests of the composites were performed according to BS EN 2561 (1995) while the pure epoxy plates were tested in accordance with ASTM D638 (2014). The neat (powder) epoxy tensile properties served as a common reference line (matrix). The average tensile modulus and strength of the epoxy plates (dog-bones) were ~3GPa and ~73 MPa, respectively, as displayed in Table 2. Clearly, the 50C-epoxy matrix laminates present higher tensile strength and modulus than those of the F0E-epoxy and the 60E-epoxy where the differences in strength and modulus between the latter two composites were not significant. The obtained results suggest that the higher degree of straightness for the 50C composite ($f_{50C,tension} \approx 0.95 > f_{F0E,tension} \approx 0.92 > f_{60E,tension} \approx 0.89$, where f is the direction parameter [30]) and the fact that the 50C fibre consisted of the largest amount of sizing, resulted in an improvement of the interfacial adhesion strength between the components, thus the best tensile performance. It is worth pointing out that according to

Mulvihill et al. [41], fibre-fibre and tow-on-tow friction contributions should be also taken into account as the fibre type with the highest sizing amount i.e., the 50C case, revealed the highest friction coefficient; thus, the highest interface strength was expected. As such, the interfacial bonding between the carbon fibres and the powder epoxy were clearly affected by the fibre straightness, and friction forces [41] which are closely related to the amount of sizing on the fibres' surface (although differences in sizing chemistry may also affect the bond strength). Note that the tensile results obtained for the composites in this investigation were similar to property data of the Toray composite cases as reported by the manufacturer's datasheet [42] and presented in Table 2.

Table 2 Mean tensile properties in the longitudinal direction for the three types of CFRPs (and neat epoxy) and the Toray composites with FVF of 60% [42]. Note that over 6 tests were performed for each composite case and the tensile results of the fabricated composites were normalised to 58% FVF for means of comparison.

Material	**Strength (MPa)**	**Modulus (GPa)**
50C CF/epoxy	2600±120	132±4.1
F0E CF/epoxy	2310±100	124±2.8
60E CF/epoxy	2172±105	119±3.1
Toray CF/epoxy [42]	2550	135
Powder epoxy	73.1±2.9	3.0±0.5

3.4 Flexural properties

0° flexural tests of the three different UD composite cases (all manufactured under tension conditions) and the neat (powder) epoxy plates were performed, and the results are plotted in Fig. 7. To properly evaluate the flexural performance of the composites, the fibre volume fractions are needed. The FVF was found to be 58±3% for all examined composites. In Fig. 7(A), the measured flexural strengths for the 50C (~1180 MPa) and F0E (~1068 MPa) cases are higher than that for the 60E composite (~960 MPa). Note that the flexural strength results of the unreinforced epoxy specimens were not plotted in Fig. 7, as the flexure tests were optimised for testing composites materials (ASTM D7264) and not rigid plastics. During the flexural tests of the epoxy plates, it was found that they yielded too easily to the limit of the test deflection range. Fig. 7(B) shows the results obtained for the flexural moduli for the T700S family of composites and for the neat epoxy plates. The flexural modulus was calculated to be ~117 GPa for the 50C case, ~105 GPa for the F0E case, and ~98 GPa for the 60E case. It is clear that the 50C composites obtained the highest modulus and strength of the three composites in agreement with the obtained 0° tensile tests. Considering that all three types of fibres have similar mechanical properties [42], the same matrix, as well as approx. similar FVF, the differences observed in the flexural properties were attributed to the different sizing agents i.e., amount (and type). This resulted in varying degrees of interfacial bonding between the fibres and matrix, for each composite case. Additionally, as reported by Mamalis et al. [30], the resulted varying degree of fibre straightness (50C>F0E>60E) due to the tensioning conditions applied to the three fibre types, during their cure cycle, with respect to the amount of sizing, was most likely to influence the fibre-fibre and tow-tow interactions in the composites, and so also the interfacial bond strength between fibres and matrix. It has to be noted that the friction forces between the fibres and the tows may also play an important role by improving the adhesion strength of the system as reported by Mulvihill et al. [41]. Historically, interfacial bond strength has been shown to drastically influence the ultimate flexural performance of UD composites [30,64]. Thus, in our cases, the 0-degree flexural strength and stiffness increased with the thickness of the sizing agent (as the latter increased fibre straightness, and this caused better stress transfer to the fibres). Note that the flexural strength of the Toray [42] composite (data provided from the respective manufacturers) was higher than all the examined composite cases in this study, while the flexural modulus was found to be in the same range. This suggests that the differences observed in the flexural properties between the presented cases and the TORAYCA® composite, were most likely due to a) the different matrices used between the datasheet (with different cure temperatures) and the present experiments, b) the different lay-up techniques adopted and c) the low compressive strength of the composites, as reported by Murray et al. [65].

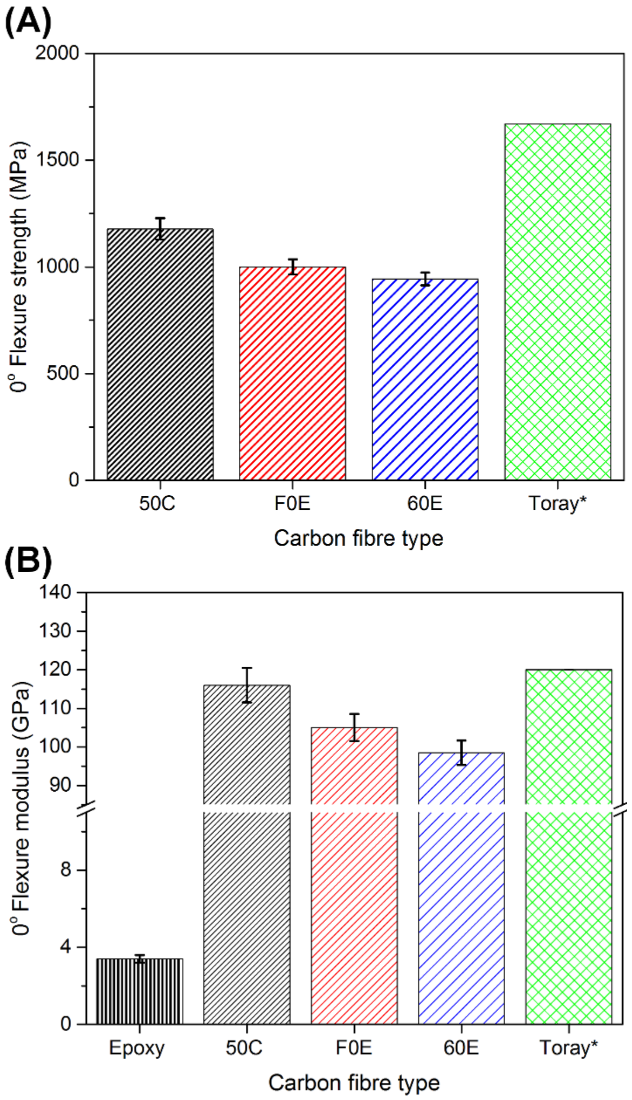

Fig. 7. Longitudinal flexural (A) strength and (B) modulus results for the T700S composite family, manufactured under tensioning conditions, as well as the modulus for the neat (powder) epoxy. The flexural results are average values from around 12 tests for each case. The obtained results were normalised at ~58% FVF for means of comparison. Note that the flexural results for the Toray composite (FVF ~60%) were provided from the manufacturers as a means of comparison [42]. Error bars indicate the experimental standard deviation.

3.5 Flexural fracture characteristics

A fractographic analysis was performed on the cross sections of the flexural test specimens to scrutinise the effect of different sizings on the CF surfaces (and so, interfacial bonding variations) on the failure mechanisms of the different composite cases. Fig. 8 shows typical optical microscopy and SEM images of the flexure fracture surfaces, for the three composite cases, respectively. In Fig. 8 (A) – (C), the fibres were oriented in a parallel manner to the cross section plane, whereas in the SEM images of (D) – (F), the fibres were oriented perpendicularly to the cross section plane of the specimens. In all cases, the first layers of CFs, which were directly subjected to the applied load, were completely crushed and broken down. There were no signs of delamination in the F0E and 60E specimens, and the layers were well connected to each other after failure. This seemed to confirm strong interfacial bonding between the reinforcing fibres and epoxy matrix. However, the failure behaviour of the 50C case, presented in Fig. 8(A), was characterised by fibre breakage in the upper layers as well as some matrix cracking. In addition, a few minor delaminations were observed, albeit at the higher flexural load imposed on this composite family, as seen in Fig. 7(A). The higher flexural load required for the fracture of the 50C specimen during the 4-point bending test deteriorates the interfacial bonding between the carbon fibres and matrix leading to partial delamination in the structure. Furthermore, failure in the form of matrix cracking, was attributed to the higher elastic modulus of the 50C composite due to its higher amount of sizing agent, which enables the matrix/interface to bear higher loads compared to the other composites. It should be noted that in the 50C and F0E cases, and less prominently in the 60E case, the compressed region was raised due to kinking, causing a local increase in cross sectional area, peaking at the fracture surface.

Similar failure patterns across the surfaces of the specimens can be observed in the SEM images in Fig. 8 (D) – (F). A clear demarcation of tension and compression regions can be identified with the neutral axis separating these two regions. The rough area indicates tensile fracture while the smooth area refers to compressive fracture. The flexural failure has originated on the compression surface due to the lower strength of CFRP in compression relative to tension and the stress concentration generated by the two loading blocks of the test fixture. In Fig. 8 (D) – (F), it is clear that crack propagation started from the upper surface, growing towards the neutral axis. At this stage the crack moved into a field of decreasing compressive stress and increasing interlaminar shear stress, which in turn stopped the compressive fracture. An increase in tensile strain due to delamination in the opposite face initiated rapid failure towards the neutral zone, concurrently [66,67]. As the moduli for compression and tension are similar [65], the neutral axis would have originally been located in the middle of the specimen's thickness during elastic deformation, in all cases. However, due to the significantly inferior compressive strength, as plastic deformation and crack growth occurred in the compressive region, this neutral axis of bending likely shifted towards the tensioned region. Images of the failed flexural samples prior to separation confirmed that approximately 60 – 70% of failure was in compression. Shear failure occurred in the 60E case at the neutral axis where shear stresses were dominant while minor delamination occurred in the compressed region for the 50C case. These are common failure types which have been well reported in literature for tested composites under bending mode [68,69]. While little distinction between cases can be observed at low magnifications for the tensioned region, higher magnification images show the effects of fibres sizings (and fibre straightness) on failure in tension.

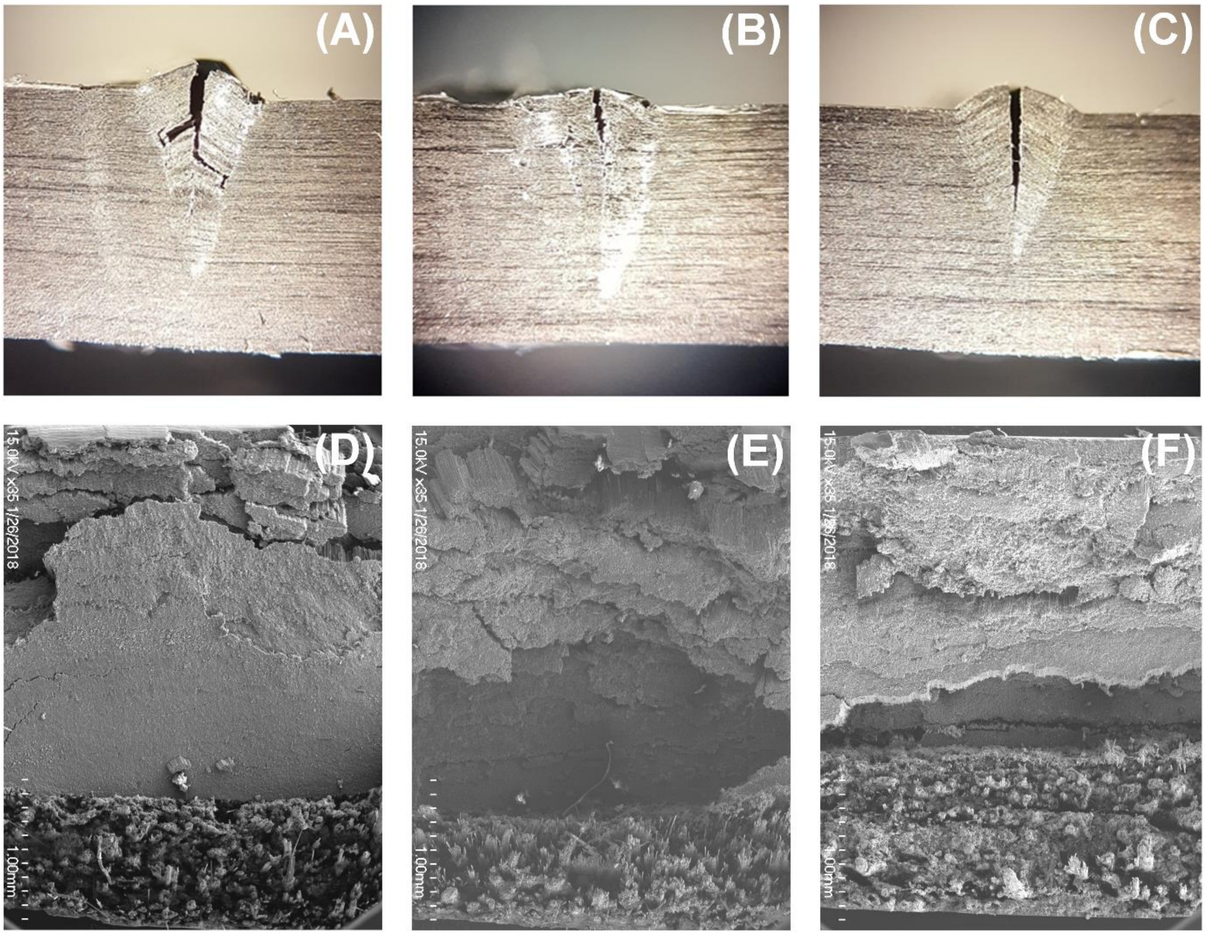

Fig. 8. Cross sectional microscopy images of (A) 50C, (B) F0E and (C) 60E fractured specimens, with fibre running horizontally. SEM images of the fracture surfaces after four-point bending for (D) 50C, (E) F0E and (F) 60E with fibres running transverse to the plane of the image. Note tensile failures on the lower part of the SEM images, with compressive failures above the neutral axis.

Moreover, high-magnification SEM images of the distinct tensioned regions were captured to determine variations between the three composite cases. By visual comparison of the tensioned regions in Fig. 9, in all CFRP cases, carbon fibres were covered by epoxy, indicating good wettability and subsequently good interfacial bonding properties. However, in Fig. 9(B), a fibre pull-out fracture can be observed, characteristic of adhesion failure, illustrating lower compatibility of the sized fibre with the matrix system in comparison with the other CFRP cases, where cracks were seen to propagate in the epoxy matrix resulting in cohesive failure. The surface fracture characteristics observed in F0E composite case are in agreement with the sizing compatibility of the F0E carbon type as specified from the manufacturers and reported in literature [30]. Arguably, if the interface bonding between fibre and resin was not strong enough, the crack in the composite specimens would propagate along the interface. However, the observed cracks in laminates with very strong interfaces propagated preferentially in the vertical direction. The tensioned surface of the 60E composite showed that the matrix was fully covering the fibres, similar to previous cases, but with a more severe disorientation of fibres owing to the lower degree of fibre straightness compared to other cases [30], as displayed in Fig. 9(C). In summary, the fractographic analyses of the three composite cases enabled better understanding of a) the nature of the failure of the specimens, b) the effect of different sizing agents on interfacial interactions (bond strength) and c) the load distribution between the epoxy matrix and the reinforcement for each case.

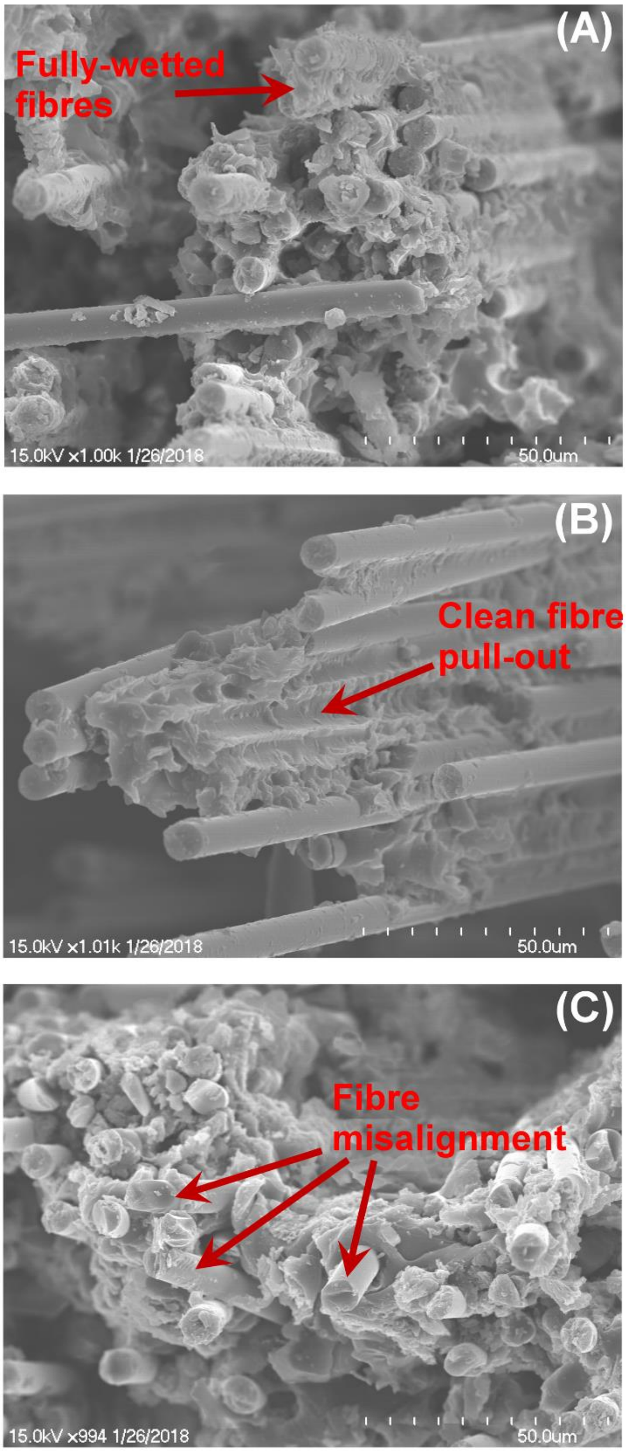

Fig. 9. High-magnification SEM images of the fracture surface of the (A) 50C, (B) F0E and (C) 60E tested/failed CFRPs, after four-point bending.

3.6 Interlaminar fracture toughness

The interlaminar fracture toughness was determined as the Mode-I critical strain energy release rate (per unit area) i.e., G_{IC}. The crack length and apparent G_{IC} values were obtained from the high-speed image sequences of each DCB test, which were recorded at approx.1000 frames per second. The symmetry of both cantilever beams (loading blocks) was maintained during the test. Typical load–displacement curves of the interlaminar fracture tests for the three different carbon fibre-reinforced epoxy composites are shown in Fig. 8. The stiffness of each specimen is represented by the slope of the load-displacement curves for each composite. For all composite cases, the load increased linearly until it reached a maximum value where the crack initiated (at around 63 mm), and then a gradual decrease of the load followed as the crack further propagated. Characteristic stick-slip behaviour in all composite cases was observed which was possibly due to variations in local material topology, such as resin-rich or fibre-rich regions along the longitudinal direction, slight misalignment of the fibres or the presence of voids, as well as the fracture of bridged fibres or fibre bundles. It is worth noting that material variations cannot be completely avoided, although care was taken during the fabrication process (hand lay-up technique) to minimise them. In all cases (Fig. 10), the load slightly drops at several points after the peak load, corresponding to a stable and slow crack propagation mechanism. The curves consist of repetitive small load drops followed by a gradual increase of the load (Fig. 10). In the majority of the cases, delamination propagated in a stable and gentle manner for a short distance, and then it was halted. After sufficient continued loading, the crack reinitiated. Therefore, the crack propagated in a series of small jumps accompanying the slight load drops. The curves, in Fig. 10, show that the load needed to initiate delamination was greater for the 50C CFRP case, than for 60E and F0E composite cases. The highest critical load that was observed for the 50C case was about +15% and +30% higher than the 60E and F0E composites, respectively. Note that all composites revealed a smooth (gentle) stick-slip behaviour but at different load magnitudes. Detailed examination of the tested samples revealed that the crack propagated in the main delamination plane without any side cracking and branching. Furthermore, the stiffness for the composite cases was observed to decrease in the order (50C>60E>F0E) which was attributed to the varying degrees of interfacial bonding between the fibres and the (powder) epoxy owing to the different amount (and type) of sizing agent on the surface of the fibres. It may be observed that in almost all tested samples an initial non-linear region was observed (Fig. 10). The latter was due to the initial take-up portion of load introduced and the simultaneous opening of the pre-crack area of specimens prior to crack initiation.

The results of the Mode-I DCB tests for all different types of composites are summarised in Fig. 11. The G_{IC} values refer to averages obtained from the strain energy released during crack initiation and propagation according to ASTM D5528 (MBT). The overall Mode-I interlaminar fracture toughness values of the 50C composite ($G_{IC} \approx 1610$ J/m^2) were higher than those of the 60E ($G_{IC} \approx 1310$ J/m^2) and F0E ($G_{IC} \approx 1120$ J/m^2) cases, which means that the ability of the 50C composite to contain a crack and resist fracture was superior to those of the 60E and F0E composites. A related point is that the F0E sizing is designed for vinyl ester resins and it is also compatible with epoxy systems as specified by the manufacturers [43] and reported in previous studies [70]. The latter argument was also reported by Mamalis et al. where the distribution of functional groups on the F0E carbon surface, using Fourier transform infrared spectroscopy (FTIR), was found to be slight different compared to 50C and 60E indicating a different polymeric blend presented on the surface of the F0E carbon fibres [30]. In turn, different chemical interlocking phenomena were expected for the F0E case compared to the 50C and 60E ones, with respect to the amount of sizing and the degree of fibre straightness. The latter was evident for the F0E composites during DCB tests where the fracture energy released was substantial lower than the other cases indicating weaker interfacial bonding. This was also revealed in the previous work of Mamalis et al. [30] where the FOE composite case achieved the lowest transverse flexural strength pointing out the relatively weak bond strength between fibre/matrix, even though the amount of sizing for FOE carbon type was significant higher than the 60E carbon fibres.

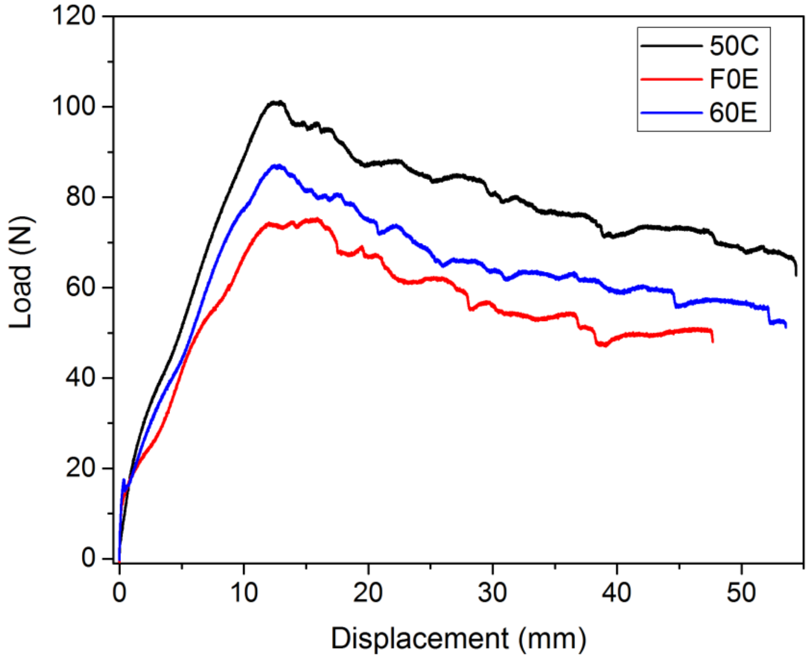

Fig. 10. Representative (Mode-I DCB) load-displacement curves of the CFRPs reinforced with three different types of carbon fibres.

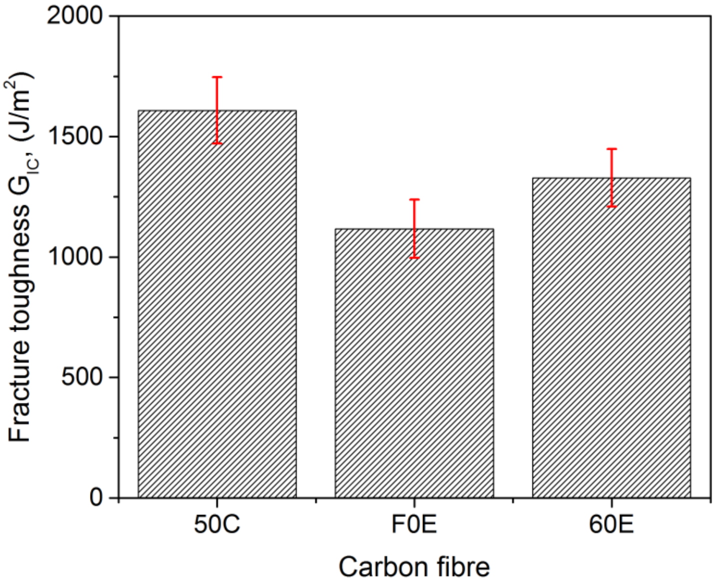

Fig. 11. Comparison of Mode-I fracture toughness results for the three different CFRP cases. The average values were calculated from over ~7 tests for each composite case. Error bars indicate the experimental standard deviation.

From each load-displacement curve, the critical load (N) and displacement (mm) can be determined for a number of crack lengths. In turn, these values were substituted into Eq. (1) to determine the Mode-I interlaminar fracture toughness, G_{IC}. In Fig. 12(A), the calculated G_{IC} values were plotted as functions of the delamination growth i.e., as a resistance curve (R-curve). The R-curves shown in Fig. 12 are representative examples for the three composites cases (as portrayed in Fig. 10) and do not correspond to the values seen in the bars in Fig. 11, which represent the average fracture energy measured for over ~7 samples for each composite type. As expected, the largest Mode-I fracture toughness was observed in 50C case compared to the other composite i.e., F0E and 60E, in terms of their critical load. The Mode-I fracture toughnesses reported here are average strain energies released during initiation (G_{IC-I}) and propagation (G_{IC-P}), with the onset of nonlinearity being used to evaluate the G_{IC-I} values. The G_{IC-P} values (fracture resistance) were calculated by averaging all G_{IC-R} values of all the recorded points when the delamination length was increased from ~63mm to ~88 mm. A comparison of the G_{IC-I} and G_{IC-P} values obtained for the three CFRPs are presented in Fig. 12(B), respectively. Note that the average and standard deviation values of G_{IC-I} and G_{IC-P} were obtained from the experimental results of around 7 samples for each CFRP case. Additionally, the results demonstrated that the overall magnitude of the G_{IC-P} tends to increase compared with G_{I-I} and different trends of improved fracture toughness are observed for all composites.

It is clear that the interlaminar fracture toughness properties of the three composite cases were connected to the different interfacial bonding between the fibres and matrix in each composite owing to the varying amount (and type) of sizing agents as well as the varying degree of fibre straightness as reported by Mamalis et al. [30]. Friction contributions related to fibre-fibre and tow-on-tow interactions must also be taken into account according to Mulvihill et al. [41], as they can effectively alter the adhesion strength of the involved constituents. Additionally, Fig. 11 shows typical high frame rate images of the three different composite cases from the Mode-I test. The composites were characterised by distinctive delamination features. This reflected the initiation and propagation mechanisms of the samples, which in turn determined the resistance to fracture. The fibre bridging was visible with the naked eye in all composite cases but to a different degree, as can be seen in Fig 13. Furthermore, it was observed that the debonded length of the bridging filaments became longer as the crack opening increased. More specifically, for the 50C case (Fig. 13(A)), the region behind the crack opening, over which the fibres were bridging, is not very large in comparison with the 60E and F0E cases. Hence, the 50C fibres broke almost immediately after the crack opening, indicating strong interfacial bonding for the 50C CFRP in agreement with the G_{IC}, tensile and flexural results. Additionally, Fig. 13(C) shows a photograph of a delaminating DCB specimen of the F0E case highlighting the fibre bridging in the wake of the delamination front. In this composite case, the observed extensive fibre bridging at the wake of crack front was responsible for a weak fracture resistance due to a weaker interface bond [71,72]. Fibre bridging due to interfacial debonding occurred not only at the main plane of delamination, but also at neighbouring fibre layers and interlayers, allowing increased matrix deformation [71–73]. No fracture of the bridging fibres was observed at the end of the DCB tests, which in turn clearly distinguished F0E composite from the other two. This system had the potential of unlimited fibre bridging, as the low interface bond strength caused fibres to continuously peel away from the matrix during increasing crack opening [74]. The 60E case (Fig. 13(B) was seen to follow an intermediate behaviour where the visible fibre bridging was most likely occur due to the weak interface bonding compared to 50C case (but higher than the F0E case), the higher fibre misalignment compared to the other tensioned composites [30] and lower amount of polymeric coating on the fibre surface. It worthwhile noting, that the fibre bridging phenomenon is recognised as beneficial to the G_{IC} of CFRPs, although in this paper its effect was subordinate to the enhanced interface bonding due to the sizing amount, high degree of fibre straightness and frictions contributions. This is to say, the 50C case revealed the best interlaminar fracture resistance performance due to the highest amount of sizing, highest degree of fibre straightness [30] among the tensioned composite cases (and highest friction forces between the CFs [41]) which in turn resulted in a better interface bond performance.

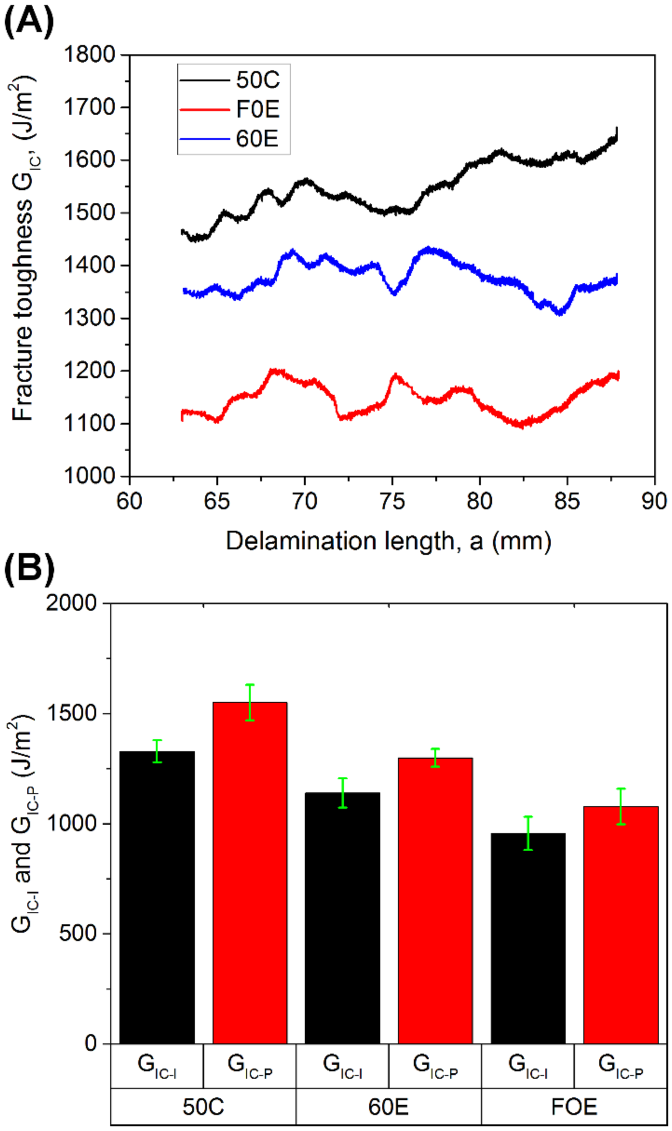

Fig. 12. (A) Representative R-curves for each composite case. (B) comparison of G_{IC-I} and G_{IC-P} (average) values of the different types of carbon fibre composites.

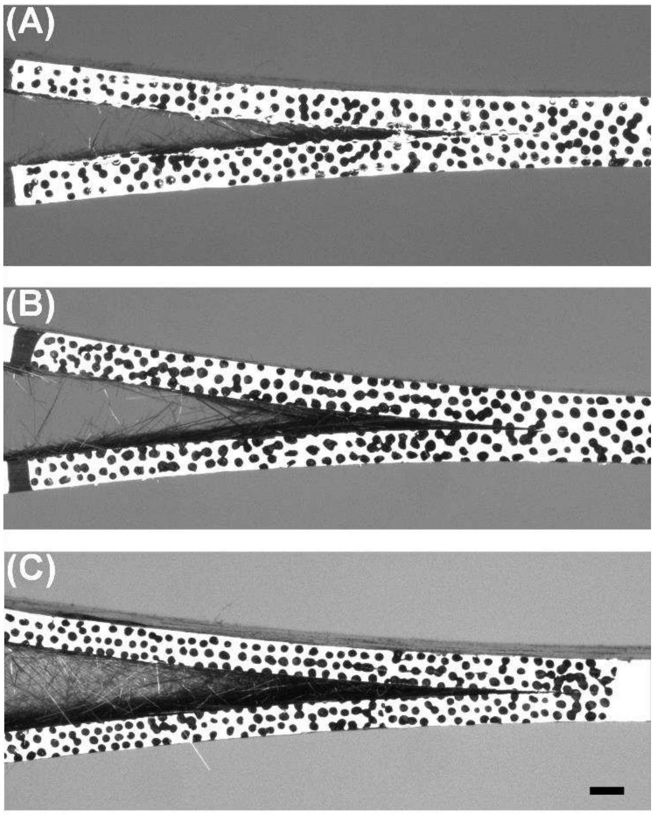

Fig. 13. Typical high-speed images of the crack tip zone in detail for the (A) 50C, (B) 60E and (C) F0E composite cases. Note that the scale bar depicts a width of 1.5 mm.

4. Conclusions

In this study, unidirectional FRPs made from reinforced carbon fibres with three types of sizing agents (50C, F0E and 60E) were manufactured, under controlled tensioning conditions. AFM and Raman spectroscopy measurements were performed to characterise the surface topography and coverage of the three carbon fibre sizings. The results demonstrated that the different amounts (and types) of sizing agents significantly changed the carbon fibres' surface morphologies and subsequently the interfacial interactions. More specifically, it was shown that the surface roughness of the carbon fibres increased with increasing amounts of sizing, enhancing not only chemical but mechanical interlocking phenomena with the powder epoxy. Friction contributions between fibre-fibre and tow-on-tow interactions would also have contributed to improved interfacial performance, (in addition to the higher amount of sizing and the higher degree of fibre straightness) resulting in higher adhesion strength and better bonding. The highest amount of sizing (~1%) was applied on the surface of the 50C fibres, producing the roughest surface profile, the strongest interfacial bonding between fibre/matrix, and the best mechanical properties of the composite types tested. A comparison of the tensile strength and tensile modulus values between the different composites revealed that both properties were highest for the 50C composite case. The latter was due to its stronger interfacial bonding and higher degree of fibre straightness in agreement with the results reported by Mamalis et al. [30]. Additionally, the tensile performance of the neat (powder) epoxy were evaluated as a reference baseline. Similarly to the tensile results, 0^{o} flexural tests revealed that the 50C case was characterised by superior performance, both in strength and modulus compared to the F0E and 60E cases. Furthermore, it was shown from fractographic analysis that slight differences existed in the flexural fracture surfaces of the three composites. However, the fracture mechanisms for each composite case, under 4-point bending mode, were different in each case, and rather complex. Delaminations and shear failure were observed in the 50C case in the compressed region, unlike the other cases. The effect of varying interfacial bonding on the interlaminar mechanical properties of CFRPs was investigated with respect to the sizing amount and the degree of fibre straightness. Friction contributions were also taken into consideration in accordance with Mulvihill et al. [41] as they can effectively enhance adhesion strength of the between fibres, tows and interlayers. The experimental results of DCB tests demonstrated that the Mode-I interlaminar fracture toughness of the 50C composites was the highest compared with the other cases due to the stronger bond strength between the fibre and the matrix and so between the inter-plies. The crack propagation paths of the three composites presented different propagation modes with distinct characteristics, providing useful information regarding the relationship between the improved interlaminar fracture toughness and interfacial bond strength in association with the varying degree of fibre straightness in the CFRPs. The above results may have important implications for the use of powder epoxy composites that enables a new generation of low-cost out-of-autoclave processes to be deployed and manufacturing costs to be reduced.

Acknowledgments

This work was carried out with funding from MARINCOMP, Novel Composite Materials and Processes for Marine Renewable Energy, funded under: EU FP7-People, Industry Academia Partnerships and Pathways (IAPP), Project reference: 612531. We also acknowledge funding from POWDERBLADE, Commercialisation of Advanced Composite Material Technology: Carbon-Glass Hybrid in Powder Epoxy for Large Wind Turbine Blades, funded under: Horizon 2020, Fast Track to Innovation Pilot, Project reference: 730747. The authors thank Composites Testing Laboratory (Ireland), for performing a series of tests. The authors are also thankful to

Dr. Vassilis Papadakis and Dr. George Kenanakis from Photonics, Phononics, and Meta-Materials (PPM) Lab Institute of Electronic Structure and Laser (IESL), Foundation for Research & Technology - Hellas (FORTH), for helping with Raman spectroscopy. J. McClements acknowledges the SOFI CDT (EPSRC, Grant Ref. No. EP/L015536/1) for financial support.

References

[1] Agrawal S, Singh KK, Sarkar PK. Impact damage on fibre-reinforced polymer matrix composite - A review. J Compos Mater 2014;48:317–32. doi:10.1177/0021998312472217.

[2] Yao L, Li M, Wu Q, Dai Z, Gu Y, Li Y, et al. Comparison of sizing effect of T700 grade carbon fiber on interfacial properties of fiber/BMI and fiber/epoxy. Appl Surf Sci 2012;263:326–33. doi:10.1016/j.apsusc.2012.09.054.

[3] Carlsson LA, Adams DF, Pipes RB. Experimental Characterization of Advanced Composite Materials. 2012. doi:10.1201/NOE1587161001.

[4] Chung DDL. Carbon fiber composites. Butterworth-Heinemann; 1994.

[5] Yu K, Shi Q, Dunn ML, Wang T, Qi HJ. Carbon Fiber Reinforced Thermoset Composite with Near 100% Recyclability. Adv Funct Mater 2016;26:6098–106. doi:10.1002/adfm.201602056.

[6] Liu X, Wang R, Wu Z, Liu W. The effect of triangle-shape carbon fiber on the flexural properties of the carbon fiber reinforced plastics. Mater Lett 2012;73:21–3. doi:10.1016/j.matlet.2012.01.003.

[7] Giurgiutiu V. Damage and Failure of Aerospace Composites. Struct. Heal. Monit. Aerosp. Compos., 2016, p. 125–75. doi:10.1016/B978-0-12-409605-9.00005-2.

[8] Bassyouni M, Gutub SA. Materials selection strategy and surface treatment of polymer composites for wind turbine blades fabrication. Polym Polym Compos 2013;21:463.

[9] Mishnaevsky L, Branner K, Petersen HN, Beauson J, McGugan M, Sørensen BF, et al. Materials for Wind Turbine Blades: An Overview. Mater (Basel, Switzerland) 2017;10. doi:10.3390/ma10111285.

[10] Morgan P. Carbon Fibers and Their Composites. CRC Press, Boca Raton, FL, USA; 2005.

[11] Rezaei F, Yunus R, Ibrahim NA. Effect of fiber length on thermomechanical properties of short carbon fiber reinforced polypropylene composites. Mater Des 2009;30:260–3. doi:10.1016/j.matdes.2008.05.005.

[12] Salam MBA, Hosur M V., Zainuddin S, Jeelani S. Improvement in Mechanical and Thermo-Mechanical Properties of Epoxy Composite Using Two Different Functionalized Multi-Walled Carbon Nanotubes. Open J Compos Mater 2013;03:1–9. doi:10.4236/ojcm.2013.32A001.

[13] Pilato LA, Michno MJ. Advanced Composite Materials. 2014. doi:10.1007/s13398-014-0173-7.2.

[14] Alessi S, Pitarresi G, Spadaro G. Effect of hydrothermal ageing on the thermal and delamination fracture behaviour of CFRP composites. Compos Part B Eng 2014;67:145–53. doi:10.1016/J.COMPOSITESB.2014.06.006.

[15] Lee DG, Lee CS, Lee HG, Hwang HY, Kim JW. Novel applications of composite structures to robots, machine tools and automobiles. Compos Struct 2004;66:17–39. doi:10.1016/j.compstruct.2004.04.044.

[16] Song YS, Youn JR, Gutowski TG. Life cycle energy analysis of fiber-reinforced composites. Compos Part A Appl Sci Manuf 2009;40:1257–65. doi:10.1016/J.COMPOSITESA.2009.05.020.

[17] Cartié DDR, Irving PE. Effect of resin and fibre properties on impact and compression after impact performance of CFRP. Compos - Part A Appl Sci Manuf 2002;33:483–93. doi:10.1016/S1359-835X(01)00141-5.

[18] Ma Y, Yang Y, Sugahara T, Hamada H. A study on the failure behavior and mechanical properties of unidirectional fiber reinforced thermosetting and thermoplastic composites. Compos Part B Eng 2016;99:162–72. doi:10.1016/j.compositesb.2016.06.005.

[19] Oyama HT, Sekikawa M, Shida S. Effect of the interface structure on the morphology and the mechanical, thermal, and flammability properties of polypropylene/poly(phenylene ether)/magnesium hydroxide composites. Polym

Degrad Stab 2012;97:755–65. doi:10.1016/J.POLYMDEGRADSTAB.2012.02.005.

[20] Mesogitis TS, Skordos AA, Long AC. Uncertainty in the manufacturing of fibrous thermosetting composites: A review. Compos Part A Appl Sci Manuf 2014;57:67–75. doi:10.1016/J.COMPOSITESA.2013.11.004.

[21] Zhan-Sheng Guo Z-S, Ling Liu L, Bo-Ming Zhang B-M, Shanyi Du S. Critical Void Content for Thermoset Composite Laminates. J Compos Mater 2009;43:1775–90. doi:10.1177/0021998306065289.

[22] de Almeida SFM, Neto Z dos SN. Effect of void content on the strength of composite laminates. Compos Struct 1994;28:139–48. doi:10.1016/0263-8223(94)90044-2.

[23] Liu L, Zhang B-M, Wang D-F, Wu Z-J. Effects of cure cycles on void content and mechanical properties of composite laminates. Compos Struct 2006;73:303–9. doi:10.1016/J.COMPSTRUCT.2005.02.001.

[24] Zhu H, Wu B, Li D, Zhang D, Chen Y. Influence of Voids on the Tensile Performance of Carbon/epoxy Fabric Laminates. J Mater Sci Technol 2011;27:69–73. doi:10.1016/S1005-0302(11)60028-5.

[25] Carraro PA, Maragoni L, Quaresimin M. Influence of manufacturing induced defects on damage initiation and propagation in carbon/epoxy NCF laminates. Adv Manuf Polym Compos Sci 2015;1:44–53. doi:10.1179/2055035914Y.0000000004.

[26] Belder E., Rutten HJ., Perera D. Cure characterization of powder coatings. Prog Org Coatings 2001;42:142–9. doi:10.1016/S0300-9440(01)00149-7.

[27] Maguire J, Roy AS, Doyle D, Logan M, O Brádaigh C. Resin Characterisation for Numerical Modelling of Through-Thickness Resin Flow During OOA Processing of Thick-Section Wind or Tidal Turbine Blades. Proc. ICCM20, 2015, p. 3307–2.

[28] Mamalis D, Flanagan T, Doyle A, Brádaigh CMÓ. A Carbon Fibre Reinforced Powder Epoxy Manufacturing Process for Tidal Turbine Blades. EWTEC12, 2017.

[29] Maguire JM, Nayak K, Ó Brádaigh CM. Characterisation of epoxy powders for processing thick-section composite structures. Mater Des 2018;139:112–21. doi:10.1016/J.MATDES.2017.10.068.

[30] Mamalis D, Flanagan T, Ó Brádaigh CM. Effect of fibre straightness and sizing in

carbon fibre reinforced powder epoxy composites. Compos Part A Appl Sci Manuf 2018;110:93–105. doi:10.1016/J.COMPOSITESA.2018.04.013.

[31] Schmidt S, Mahrholz T, Kühn A, Wierach P. Powder binders used for the manufacturing of wind turbine rotor blades. Part 1. Characterization of resin-binder interaction and preform properties. Polym Compos 2018;39:708–17. doi:10.1002/pc.23988.

[32] Daelemans L, van der Heijden S, De Baere I, Muhammad I, Van Paepegem W, Rahier H, et al. Bisphenol A based polyester binder as an effective interlaminar toughener. Compos Part B Eng 2015;80:145–53. doi:10.1016/J.COMPOSITESB.2015.05.044.

[33] Sharma M, Gao S, Mäder E, Sharma H, Wei LY, Bijwe J. Carbon fiber surfaces and composite interphases. Compos Sci Technol 2014;102:35–50. doi:10.1016/j.compscitech.2014.07.005.

[34] Park S-J, Seo M-K, Lee J-R. Roles of interfaces between carbon fibers and epoxy matrix on interlaminar fracture toughness of composites. Compos Interfaces 2006;13:249–67. doi:10.1163/156855406775997079.

[35] He H, Wang J, Li K, Wang J, Gu J. Mixed resin and carbon fibres surface treatment for preparation of carbon fibres composites with good interfacial bonding strength. Mater Des 2010;31:4631–7. doi:10.1016/j.matdes.2010.05.031.

[36] Wu Q, Li M, Gu Y, Wang S, Yao L, Zhang Z. Effect of sizing on interfacial adhesion of commercial high strength carbon fiber-reinforced resin composites. Polym Compos 2016;37:254–61. doi:10.1002/pc.23176.

[37] Bazhenov SL, Kuperman AM, Zelenskii ES, Berlin AA. Compression failure of unidirectional glass-fibre-reinforced plastics. Compos Sci Technol 1992;45:201–8. doi:10.1016/0266-3538(92)90080-M.

[38] Chen W, Yu Y, Li P, Wang C, Zhou T, Yang X. Effect of new epoxy matrix for T800 carbon fiber/epoxy filament wound composites. Compos Sci Technol 2007;67:2261–70. doi:10.1016/j.compscitech.2007.01.026.

[39] Song W, Gu A, Liang G, Yuan L. Effect of the surface roughness on interfacial properties of carbon fibers reinforced epoxy resin composites. Appl Surf Sci 2011;257:4069–74. doi:10.1016/j.apsusc.2010.11.177.

[40] Vautard F, Fioux P, Vidal L, Schultz J, Nardin M, Defoort B. Influence of the carbon fiber surface properties on interfacial adhesion in carbon fiber–acrylate composites cured by electron beam. Compos Part A Appl Sci Manuf 2011;42:859–67. doi:10.1016/j.compositesa.2011.03.015.

[41] Mulvihill DM, Smerdova O, Sutcliffe MPF. Friction of carbon fibre tows. Compos Part A Appl Sci Manuf 2017;93:185–98. doi:10.1016/J.COMPOSITESA.2016.08.034.

[42] TORAYCA® T700S DATA SHEET 2018. http://www.toraycfa.com/pdfs/T700SDataSheet.pdf.

[43] Toray Composite Materials America, Inc. 2018. https://www.toraycma.com/page.php?id=661.

[44] Nečas D, Klapetek P. Gwyddion: an open-source software for SPM data analysis. Open Phys 2012;10:181–8. doi:10.2478/s11534-011-0096-2.

[45] Zhang Y, Zhang Y, Liu Y, Wang X, Yang B. A novel surface modification of carbon fiber for high-performance thermoplastic polyurethane composites. Appl Surf Sci 2016;382:144–54. doi:10.1016/J.APSUSC.2016.04.118.

[46] Yao L, Li M, Wu Q, Dai Z, Gu Y, Li Y, et al. Comparison of sizing effect of T700 grade carbon fiber on interfacial properties of fiber/BMI and fiber/epoxy. Appl Surf Sci 2012;263:326–33. doi:10.1016/J.APSUSC.2012.09.054.

[47] Dai Z, Shi F, Zhang B, Li M, Zhang Z. Effect of sizing on carbon fiber surface properties and fibers/epoxy interfacial adhesion. Appl Surf Sci 2011;257:6980–5. doi:10.1016/j.apsusc.2011.03.047.

[48] Zhang RL, Huang YD, Li N, Liu L, Su D. Effect of the concentration of the sizing agent on the carbon fibers surface and interface properties of its composites. J Appl Polym Sci 2012;125:425–32. doi:10.1002/app.35616.

[49] Luo Y, Zhao Y, Duan Y, Du S. Surface and wettability property analysis of CCF300 carbon fibers with different sizing or without sizing. Mater Des 2011;32:941–6. doi:10.1016/J.MATDES.2010.08.004.

[50] Zhang RL, Huang YD, Liu L, Tang YR, Su D, Xu LW. Effect of the molecular weight of sizing agent on the surface of carbon fibres and interface of its composites. Appl Surf Sci 2011;257:1840–4. doi:10.1016/J.APSUSC.2010.08.102.

[51] Ma Q, Gu Y, Li M, Wang S, Zhang Z. Effects of surface treating methods of high-strength carbon fibers on interfacial properties of epoxy resin matrix composite. Appl Surf Sci 2016;379:199–205. doi:10.1016/j.apsusc.2016.04.075.

[52] Scott WW, Bhushan B. Use of phase imaging in atomic force microscopy for measurement of viscoelastic contrast in polymer nanocomposites and molecularly thick lubricant films. Ultramicroscopy 2003;97:151–69. doi:10.1016/S0304-3991(03)00040-8.

[53] Stark M, Möller C, Müller DJ, Guckenberger R. From Images to Interactions: High-Resolution Phase Imaging in Tapping-Mode Atomic Force Microscopy. Biophys J 2001;80:3009–18. doi:10.1016/S0006-3495(01)76266-2.

[54] Broyles NS, Verghese KN, Davis RM, Lesko JJ, Riffle JS. Pultruded Carbon Fiber/Vinyl Ester Composites Processed with Different Fiber Sizing Agents. Part I: Processing and Static Mechanical Performance. J Mater Civ Eng 2005;17:320–33. doi:10.1061/(ASCE)0899-1561(2005)17:3(320).

[55] Cançado LG, Jorio A, Ferreira EHM, Stavale F, Achete CA, Capaz RB, et al. Quantifying Defects in Graphene via Raman Spectroscopy at Different Excitation Energies. Nano Lett 2011;11:3190–6. doi:10.1021/nl201432g.

[56] Cançado LG, Jorio A, Pimenta MA. Measuring the absolute Raman cross section of nanographites as a function of laser energy and crystallite size. Phys Rev B 2007;76:064304. doi:10.1103/PhysRevB.76.064304.

[57] Ferrari AC, Robertson J. Resonant Raman spectroscopy of disordered, amorphous, and diamondlike carbon. Phys Rev B 2001;64:075414. doi:10.1103/PhysRevB.64.075414.

[58] Ferrari AC, Robertson J. Interpretation of Raman spectra of disordered and amorphous carbon. Phys Rev B 2000;61:14095–107. doi:10.1103/PhysRevB.61.14095.

[59] Okuda H, Young RJ, Wolverson D, Tanaka F, Yamamoto G, Okabe T. Investigating nanostructures in carbon fibres using Raman spectroscopy. Carbon N Y 2018;130:178–84. doi:10.1016/J.CARBON.2017.12.108.

[60] Melanitis N, Tetlow PL, Galiotis C. Characterization of PAN-based carbon fibres with laser Raman spectroscopy. J Mater Sci 1996;31:851–60. doi:10.1007/BF00352882.

[61] Chaudhuri SN, Chaudhuri RA, Benner RE, Penugonda MS. Raman spectroscopy for

characterization of interfacial debonds between carbon fibers and polymer matrices. Compos Struct 2006;76:375–87. doi:10.1016/J.COMPSTRUCT.2005.05.009.

[62] Tang B, Guoxin H, Gao H. Raman Spectroscopic Characterization of Graphene. Appl Spectrosc Rev 2010;45:369–407. doi:10.1080/05704928.2010.483886.

[63] Mignuzzi S, Kumar N, Brennan B, Gilmore IS, Richards D, Pollard AJ, et al. Probing individual point defects in graphene via near-field Raman scattering. Nanoscale 2015;7:19413. doi:10.1039/c5nr04664e.

[64] Brocks T, Cioffi MOH, Voorwald HJC. Effect of fiber surface on flexural strength in carbon fabric reinforced epoxy composites. Appl Surf Sci 2013;274:210–6. doi:10.1016/j.apsusc.2013.03.018.

[65] Murray JJ, Pappa EJ, Mamalis, D. Breathnach G, Doyle A, Flanagan T, Di Noi S, et al. Characterisation of Carbon Fibre Reinforced Powder Epoxy Composites for Wind Energy Blades. ECCM 18 –18th Eur. Conf. Compos. Mater., Athens, Greece: 2018.

[66] Greenhalgh ES, Rogers C, Robinson P. Fractographic observations on delamination growth and the subsequent migration through the laminate. Compos Sci Technol 2009;69:2345–51. doi:10.1016/J.COMPSCITECH.2009.01.034.

[67] Kozey V V. Fibre strength-dominated failure mode in unidirectional composites under compression. Mater Sci Lett 1993;12:48–52.

[68] Dong C, Davies IJ. Flexural properties of glass and carbon fiber reinforced epoxy hybrid composites. Proc Inst Mech Eng Part L J Mater Des Appl 2013;227:308–17. doi:10.1177/1464420712459396.

[69] Srinivasa V, Shivakumar V, Nayaka V, Jagadeeshaiaih S. Fracture Morphology of Carbon Fiber Reinforced Plastic Composite Laminates. Mater Res 2010;13:417–24. doi:10.1590/S1516-14392010000300022.

[70] Shivakumar KN, Swaminathan G, Sharpe M. Carbon/Vinyl Ester Composites for Enhanced Performance in Marine Applications. J Reinf Plast Compos 2006;25:1101–16. doi:10.1177/0731684406065194.

[71] Nicholls DJ, Gallagher JP. Determination of GIC in Angle Ply Composites Using a Cantilever Beam Test Method. J Reinf Plast Compos 1983;2:2–17. doi:10.1177/073168448300200101.

[72] Kim J-K, Sham M-L. Impact and delamination failure of woven-fabric composites. Compos Sci Technol 2000;60:745–61. doi:10.1016/S0266-3538(99)00166-9.

[73] Zhou J, Li Y, Li N, Hao X. Enhanced interlaminar fracture toughness of carbon fiber/bismaleimide composites via microwave curing. J Compos Mater 2017;51:2585–95. doi:10.1177/0021998316673892.

[74] Feih S, Wei J, Kingshott P, Sørensen BF. The influence of fibre sizing on the strength and fracture toughness of glass fibre composites. Compos Part A Appl Sci Manuf 2005;36:245–55. doi:10.1016/J.COMPOSITESA.2004.06.019.